International Journal of
Molecular Sciences

MDPI

Article

Genetic Ablation of Inositol 1,4,5-Trisphosphate Receptor Type 2 (IP_3R2) Fails to Modify Disease Progression in a Mouse Model of Spinocerebellar Ataxia Type 3

Daniela Cunha-Garcia [1,2], Daniela Monteiro-Fernandes [1,2], Joana Sofia Correia [1,2], Andreia Neves-Carvalho [1,2], Ana Catarina Vilaça-Ferreira [1,2], Sónia Guerra-Gomes [1,2], João Filipe Viana [1,2], João Filipe Oliveira [1,2,3], Andreia Teixeira-Castro [1,2], Patrícia Maciel [1,2,*,†] and Sara Duarte-Silva [1,2,*,†]

1 Life and Health Sciences Research Institute (ICVS), School of Medicine, University of Minho, 4710-057 Braga, Portugal; id9961@alunos.uminho.pt (D.C.-G.); id8942@alunos.uminho.pt (D.M.-F.); id8212@alunos.uminho.pt (J.S.C.); andreiacarvalho@med.uminho.pt (A.N.-C.); pg40729@alunos.uminho.pt (A.C.V.-F.); id5942@alunos.uminho.pt (S.G.-G.); id9532@alunos.uminho.pt (J.F.V.); joaooliveira@med.uminho.pt (J.F.O.); accastro@med.uminho.pt (A.T.-C.)
2 ICVS/3B's—PT Government Associate Laboratory, 4710-057 Braga/4805-017 Guimarães, Portugal
3 IPCA-EST-2Ai, Polytechnic Institute of Cávado and Ave, Applied Artificial Intelligence Laboratory, Campus of IPCA, 4750-810 Barcelos, Portugal
* Correspondence: pmaciel@med.uminho.pt (P.M.); sarasilva@med.uminho.pt (S.D.-S.)
† These authors contributed equally to this work.

Abstract: Spinocerebellar ataxia type 3 (SCA3) is a rare neurodegenerative disease caused by an abnormal polyglutamine expansion within the ataxin-3 protein (ATXN3). This leads to neurodegeneration of specific brain and spinal cord regions, resulting in a progressive loss of motor function. Despite neuronal death, non-neuronal cells, including astrocytes, are also involved in SCA3 pathogenesis. Astrogliosis is a common pathological feature in SCA3 patients and animal models of the disease. However, the contribution of astrocytes to SCA3 is not clearly defined. Inositol 1,4,5-trisphosphate receptor type 2 (IP_3R2) is the predominant IP_3R in mediating astrocyte somatic calcium signals, and genetically ablation of IP_3R2 has been widely used to study astrocyte function. Here, we aimed to investigate the relevance of IP_3R2 in the onset and progression of SCA3. For this, we tested whether IP_3R2 depletion and the consecutive suppression of global astrocytic calcium signalling would lead to marked changes in the behavioral phenotype of a SCA3 mouse model, the CMVMJD135 transgenic line. This was achieved by crossing IP_3R2 null mice with the CMVMJD135 mouse model and performing a longitudinal behavioral characterization of these mice using well-established motor-related function tests. Our results demonstrate that IP_3R2 deletion in astrocytes does not modify SCA3 progression.

Keywords: astrocyte; Machado–Joseph disease; CMVMJD135 mice; IP_3R2 KO mice; motor behavior; spinocerebellar ataxias

check for updates

Citation: Cunha-Garcia, D.; Monteiro-Fernandes, D.; Correia, J.S.; Neves-Carvalho, A.; Vilaça-Ferreira, A.C.; Guerra-Gomes, S.; Viana, J.F.; Oliveira, J.F.; Teixeira-Castro, A.; Maciel, P.; et al. Genetic Ablation of Inositol 1,4,5-Trisphosphate Receptor Type 2 (IP_3R2) Fails to Modify Disease Progression in a Mouse Model of Spinocerebellar Ataxia Type 3. *Int. J. Mol. Sci.* **2023**, *24*, 10606. https://doi.org/10.3390/ijms241310606

Academic Editor: Javier Díaz-Nido

Received: 15 May 2023
Revised: 7 June 2023
Accepted: 16 June 2023
Published: 25 June 2023

1. Introduction

Spinocerebellar ataxia type 3 (SCA3), also known as Machado–Joseph disease, is a rare autosomal dominantly inherited neurodegenerative disease [1,2] caused by an abnormal polyglutamine expansion within the ataxin-3 (ATXN3) protein [3,4]. This genetic alteration leads to slow neuronal degeneration in specific brain regions and the spinal cord, resulting in a wide variety of clinical manifestations, mainly motor-related [5–7]. Despite the well-described presence of neuronal death, other non-neuronal cells are involved in SCA3 pathogenesis [5,8–12]. Astrogliosis is a common pathological feature in SCA3 that has also been found both in humans [5,10,11,13] and in animal models [14] of the disease, suggesting an important role of astrocytes in disease pathogenesis. Astrogliosis has been considered a reaction to neuronal damage; however, studies have shown that astrocytes are activated

early in SCA3, undergoing adaptive changes at times that may precede the appearance of neuropathology [15,16]. In addition, an exploratory study of cytokines present in the blood of SCA3 patients showed that the levels of eotaxin, a cytokine secreted by activated astrocytes, were significantly lower in symptomatic SCA3 patients, while asymptomatic carriers displayed higher levels of this molecule [17]. Besides that, in SCA3 patients, reactive astrocytes are present in both spared (such as the cerebral cortex) and affected brain regions (the internal segment of the pallidum, the substantia nigra, the lateral reticular nucleus, the pontine, the pre-cerebellar nuclei, and the subthalamic nuclei [5,10,11,13]. In a mouse model of SCA3, the CMVMJD135 transgenic line [14], an increase in GFAP intensity was also found in the substantia nigra but not in the pontine nuclei, both key affected brain regions. The CMVMJD135 mouse line (hereafter referred to as Q135) was generated and characterized in our lab and has been extensively used to study SCA3 pathophysiology since it displays progressive phenotypical features and neuropathology that overlap with the clinical manifestation of SCA3 [14]. Hence, they provide a good model to study disease mechanisms in SCA3, including the involvement of astrocytes in pathogenesis.

Astrocytes are the predominant glial cell type in the central nervous system and an active participant in numerous functions in the brain, including the maintenance of homeostasis and the modulation of brain circuits [18–20]. Although astrocytes are not electrically excitable, several studies have shown that astrocytes can sense, integrate, and respond to neuronal activity by raising the intracellular calcium ion concentration [21]. It has also been demonstrated that astrocytic calcium elevations may occur spontaneously or via elicitation of neuronal activity [18,22–24]. The calcium increases are dependent not only on its entry from the extracellular space but also from its release from the intracellular storages within organelles such as mitochondria, the nucleus, and its major storing compartment—the endoplasmic reticulum (ER). While calcium from mitochondria is released via the mitochondrial permeability transition pore, calcium released from the ER occurs via ryanodine and inositol 1,4,5-trisphosphate receptors (IP_3Rs) [25–28]. The three main isoforms of IP_3Rs (IP_3R1, IP_3R2, and IP_3R3) are encoded by three distinct genes (*ITPR1*, *ITPR2*, and *ITPR3*), differing in subcellular localization, expression pattern, and functional properties [29]. The three isoforms share about 60–70% amino acid similarity [30,31]. While IP_3R1 is predominantly present in neuronal cells, IP_3R2 is mostly expressed in glial cells, e.g., astrocytes, cardiomyocytes, and hepatocytes, and IP_3R3 is present in many different cell types, e.g., epithelial cells, adult pancreatic islets cells, and gastrointestinal tract cells [32–34].

Aberrant calcium signalling has also been implicated in the pathogenesis of SCA3. Interestingly, it was shown that inhibition of calcium-dependent protease calpain suppressed the aggregation of the pathological ataxin-3 in cells and prevented neurodegeneration [35,36]. Also, mutant ataxin-3 was shown to physically interact with and disrupt the function of IP_3R1, expressed in neurons, to increase calcium release and cause Purkinje cell excitability [37]. These findings are similar to the ones described previously in animal models of HD [38–40] as well as SCA2 [41] and provide support for the assumption that several polyglutamine-expansion disorders might share common pathogenic mechanisms. Furthermore, SCA3-YAC-84Q transgenic mice fed with dantrolene, a clinically relevant calcium signalling inhibitor, showed an improvement in motor performance and prevented neuronal loss in affected brain regions, such as the pontine nuclei and the substantia nigra [37]. Thus, these results indicate that abnormal calcium signalling may play an important role in SCA3 pathology.

Calcium-dependent astrocytic functions, such as the release of gliotransmitters, rely upon the process of calcium signalling in response to neuronal activity, predominantly by IP_3R2-mediated release from internal stores [23,24,34]. Consequently, the IP_3R2 KO mouse model [42], a mutant with altered astrocytic calcium signalling due to the absence of IP_3R2, has been at the center of several relevant studies that have revealed important physiological roles of IP_3R2 signalling in not only astrocytes [43–51] but also in pathophysiological alterations in the context of stroke [52,53], traumatic brain injury [54], and some neurodegenerative diseases, such as Alexander disease [55]. The disruption of astrocytic

calcium signalling by genetically ablating IP_3R2 had a beneficial effect on neuronal protection and motor deficits after stroke [56]. On the contrary, the ablation of IP_3R2 in the context of amyotrophic lateral sclerosis was detrimental to $SOD1^{G93A}$ mice, increasing innate immunity that contributed to the significantly shorter lifespan of these animals [57]. These contradictory results have generated controversy about the functional significance of calcium signalling by IP_3R2 in astrocytes, since it has been assumed that calcium signalling is abolished in IP_3R2 KO mice [43,58,59]. However, it was later demonstrated that there is calcium signalling generated by other sources in IP_3R2 KO astrocytes [28], which may compensate to some extent for the absence of IP_3R2.

To the best of our knowledge, IP_3R2 has not been linked to SCA3 pathogenesis so far, despite evidence suggesting the involvement of astrocytes and the calcium signalling pathway in SCA3 pathogenesis. In the current study, we aimed to investigate the relevance of IP_3R2 in the onset and progression of SCA3. Here, we investigated whether IP_3R2 depletion and the consecutive suppression of global astrocytic calcium signalling would lead to marked changes in the behavioral phenotype of CMVMJD135 mice. Therefore, we crossed the CMVMJD135 mouse model [14] with the IP_3R2 KO mouse model [42] and performed an extensive longitudinal characterization of the motor phenotype of these mice using a panel of well-established behavioral tests in order to determine the effect of IP_3R2 ablation in the onset and disease presentation of SCA3.

2. Results

2.1. IP_3R2 Expression in the CMVMJD135 Mouse Model

To investigate the relevance of IP_3R2 in SCA3, we first assessed whether *Itpr2* gene expression was altered in the Q135 mice as well as to confirm IP_3R2 deletion in the double mutant animals (described here as IP_3R2 KO; Q135). We showed that the mRNA levels of *Itpr2* are not altered in the brainstem of the Q135 mouse model, a well-known affected brain region in SCA3 (Figure 1a). Importantly, and as expected, IP_3R2 is not present in the IP_3R2 KO; Q135 animals as levels of *Itpr2* mRNA in these mice were not detected (Figure 1a). To rule out the possibility that deletion of IP_3R2 could induce compensatory expression of other IP_3Rs, we assessed the expression levels of the IP_3R1 isoform. No differences were found (Figure 1b), suggesting that no adaptive compensations occurred in this constitutional KO strain, as we previously showed for the IP_3R2 KO model [51].

2.2. The Double Mutant Mice Show Progressive Neurological Deficits Similar to CMVMJD135 Animals

Next, we performed a battery of well-established motor behavioral tests to obtain a full characterization of the double mutant to determine the effect of IP_3R2 ablation in the disease presentation. In this longitudinal behavioral characterization, the animals were tested on several behavioral paradigms at 6, 8, 12, 16, 20, 24, and 30 weeks of age (Figure 2a), corresponding to early, medium, and advanced disease stages, as previously described for Q135 mice [14]. The analysis of CAG length variation revealed that the Q135 and IP_3R2 KO; Q135 mice carried a similar number of CAG repeats (Figure 2b), excluding an influence of CAG length variation on the behavior of the different test groups. All mice gained weight at a similar rate until 12 weeks of age (Figure 2c); however, the Q135 and IP_3R2 KO; Q135 mice stopped gaining weight throughout the age groups, showing a significantly lower body weight gain compared with their WT-littermates at 20, 24, and 30 weeks of age. In contrast, the control animals continued to gain weight until 30 weeks of age (Figure 2c). The IP_3R2 KO; Q135 mice displayed a lower body weight over time when compared to the Q135 mice (Figure 2c).

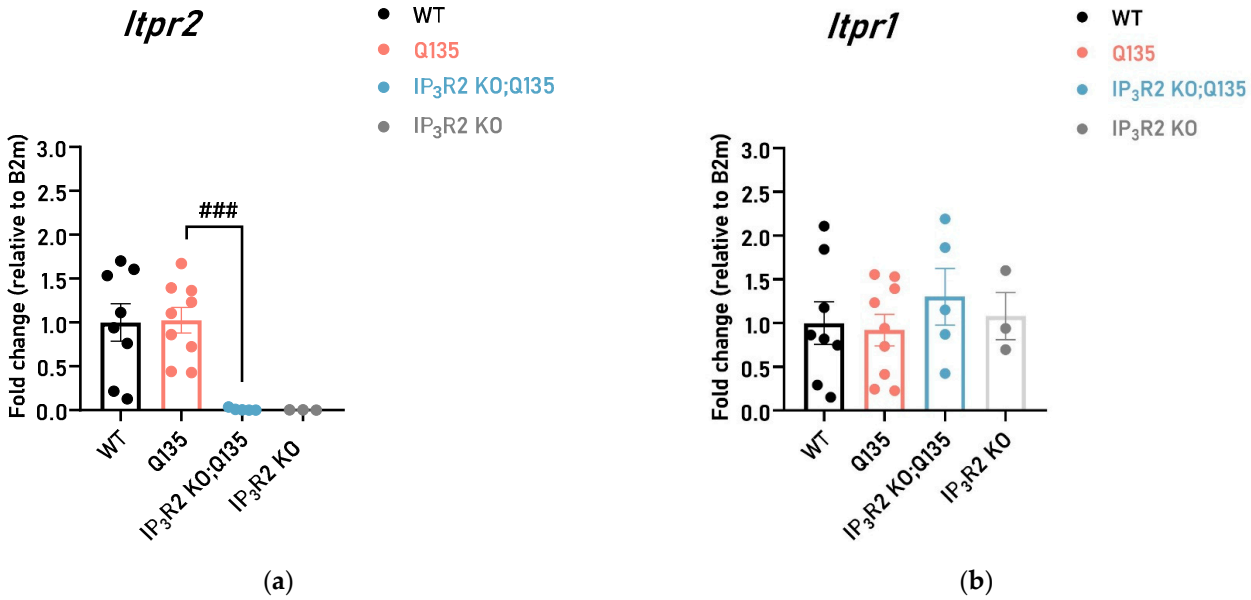

Figure 1. The relative expression of IP_3 isoforms levels in the brainstem of WT, Q135 mice, and IP_3R2 KO; Q135 mice measured by RT-qPCR. (**a**) The mRNA levels of IP_3R2 were not detected in the IP_3R2 KO; Q135 mice as expected; (**b**) No differences were found between the Q135 and IP_3R2 KO; Q135 mutant mice regarding the IP_3R1 expression levels. Relative gene expression was calculated using the $2^{-\Delta\Delta Ct}$ relative quantification method. One-way ANOVA with Tukey HSD or Dunnett T3 comparisons was carried out. All statistical information is included in Appendix A, Table A1. The data are presented as the mean ± SEM. Hashtags (###) indicate statistical significance between the Q135 and IP_3R2 KO; Q135 mice. The means were considered statistically significant at a *p*-value ### $p < 0.001$.

In the motor swimming test, no significant differences were found between the Q135 and IP_3R2 KO; Q135 mice in their swimming performance (Figure 3a), with their latency to traverse the water tank being significantly worse than that of the WT mice during aging. As the disease progresses, the Q135 mice have increasing difficulty in maintaining balance [14]. Both the Q135 and IP_3R2 KO; Q135 mice showed similar performance on the balance beams (Figure 3b–d).

Next, we evaluated whether the IP_3R2 KO; Q135 mice showed any sign of movement initiation deficits, seen as a measure of parkinsonism [60,61] a clinical feature of some SCA3 patients, with the adhesive removal test (Figure 4a). Both the Q135 and IP_3R2 KO; Q135 animals showed an increased latency to remove the nose sticker when compared to their WT-littermates, suggesting movement initiation deficits for both genotypes. Again, no differences were seen in this test between the IP_3R2 KO; Q135 and Q135 mice (Figure 4a).

Loss of muscular strength is a very early and severe symptom observed in Q135 mice, with it already being observed when the animals were 6 weeks of age [14]. Thus, forelimb and hindlimb strength were also evaluated. In the hanging wire grid (Figure 4b), the Q135 mice showed a significantly lower latency to fall from the grid when compared to their WT-littermates, suggesting that limb muscular strength is diminished in these animals. The IP_3R2 KO; Q135 mice presented a similar phenotype as the Q135 mice. Accordingly, both the Q135 and IP_3R2 KO; Q135 mice displayed lower forelimb strength measured by the wire maneuver test (Figure 4c).

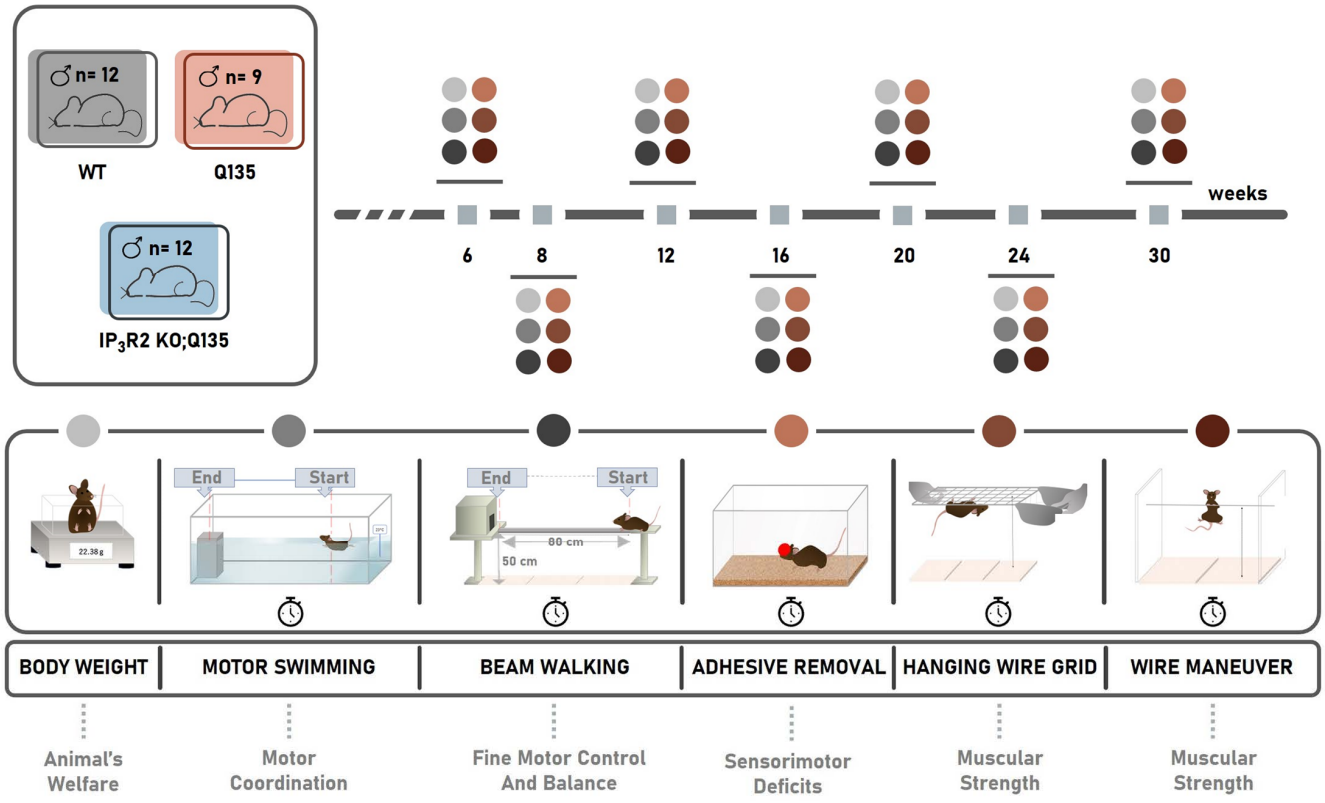

(**a**)

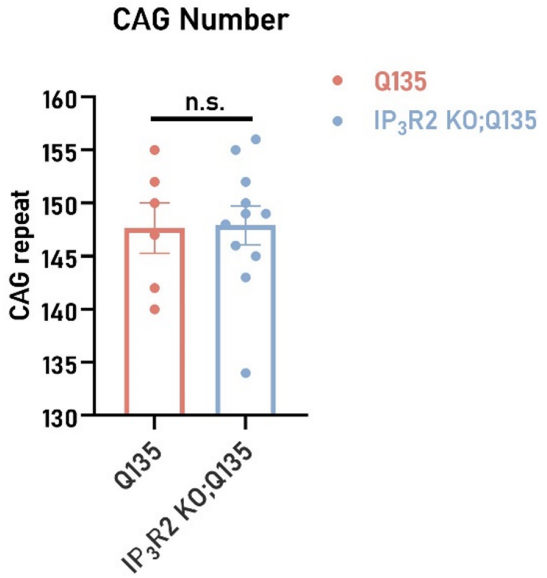

(**b**)

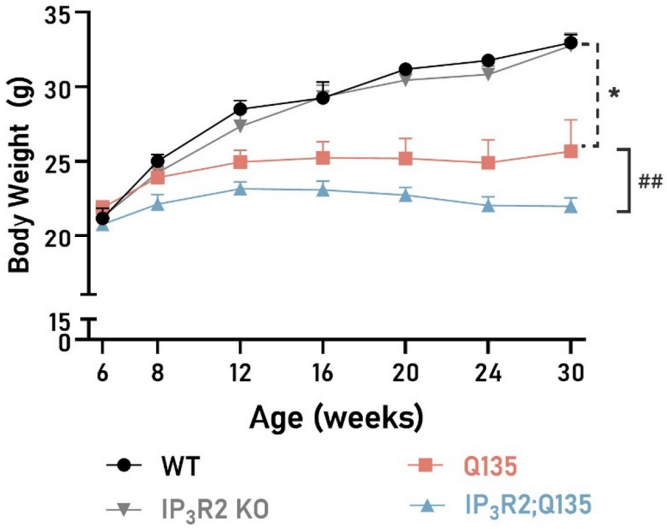

(**c**)

Figure 2. IP_3R2 ablation does not change the motor phenotype of the Q135 mice. (**a**) Schematic representation of the study design. (**b**) CAG repeat number comparison between the testing groups. (**c**) Assessment of body weight with age. An independent *t*-test, repeated measures ANOVA, and one-way ANOVA were carried out. All statistical information is included in Appendix A, Table A1. The data are presented as the mean SEM or as a percentage of animals (%). Asterisks (*) indicate statistical significance between the WT and Q135 mice, while hashtags (##) indicate statistical significance between the Q135 and IP_3R2 KO; Q135 mice. The means were considered statistically significant at a *p*-value * $p < 0.05$.

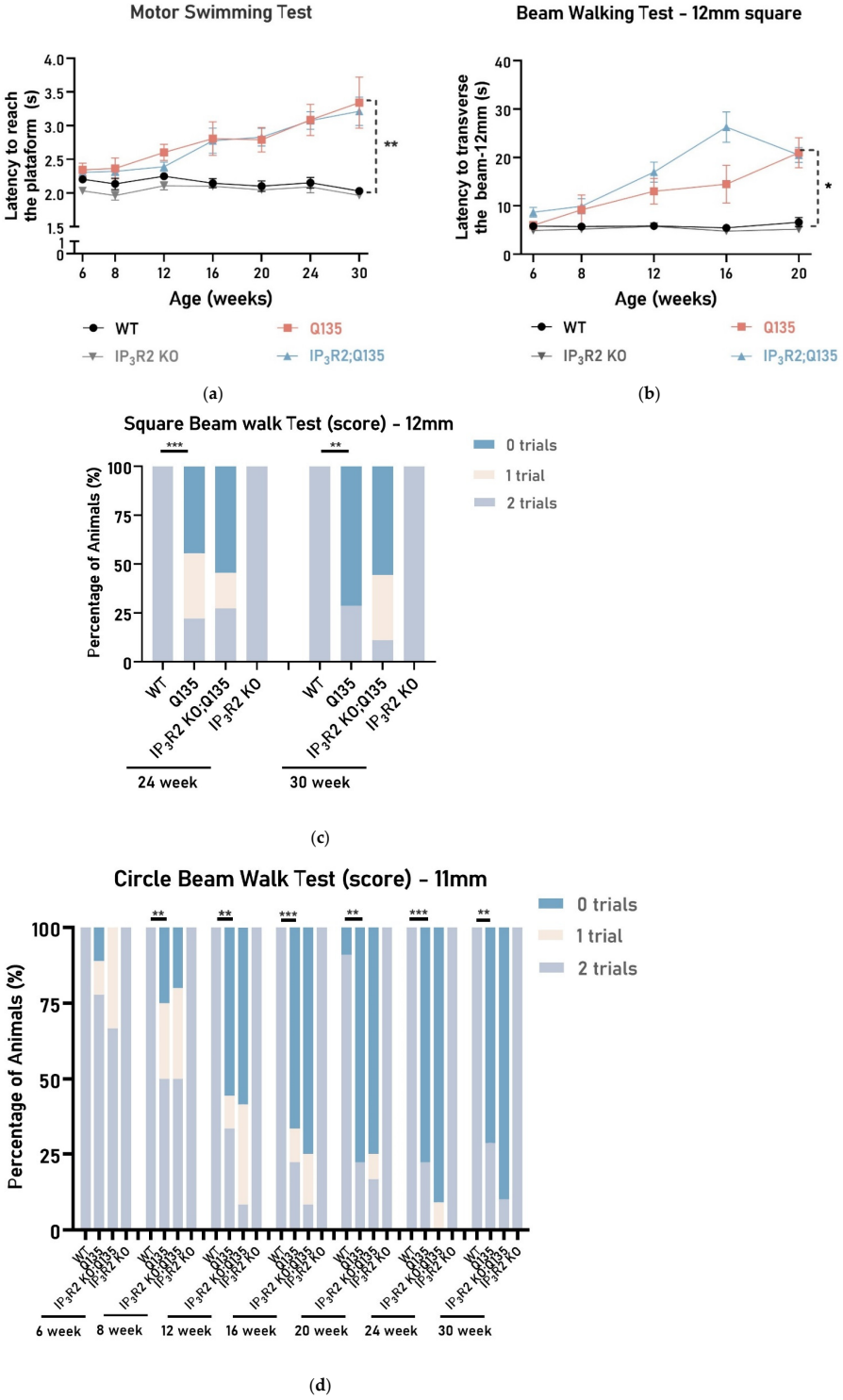

Figure 3. IP_3R2 ablation does not alter the motor performance of the Q135 mice in the behavioral tests. (**a**) In the motor swimming test, the IP_3R2 KO; Q135 animals' performance was similar when compared to the Q135 mice. The balance beam test performance of the WT, Q135, and IP3R2 KO; Q135 mice using the 12 mm square beam (**b**,**c**) and the 11 mm circle beam (**d**). Significant differences were observed in the beam walk test between the WT and the Q135 animals. However, the IP_3R2 KO; Q135 mice performed similarly to the Q135 mice. Repeated measures ANOVA, one-way ANOVA, and the Kruskal–Wallis test were carried out. All statistical information is included in Appendix A, Table A1. The data are presented as the mean SEM or as a percentage of animals (%). Asterisks (*) indicate statistical significance between the WT and Q135 mice. The means were considered statistically significant at a *p*-value * $p < 0.05$, ** $p < 0.01$, and *** $p < 0.001$.

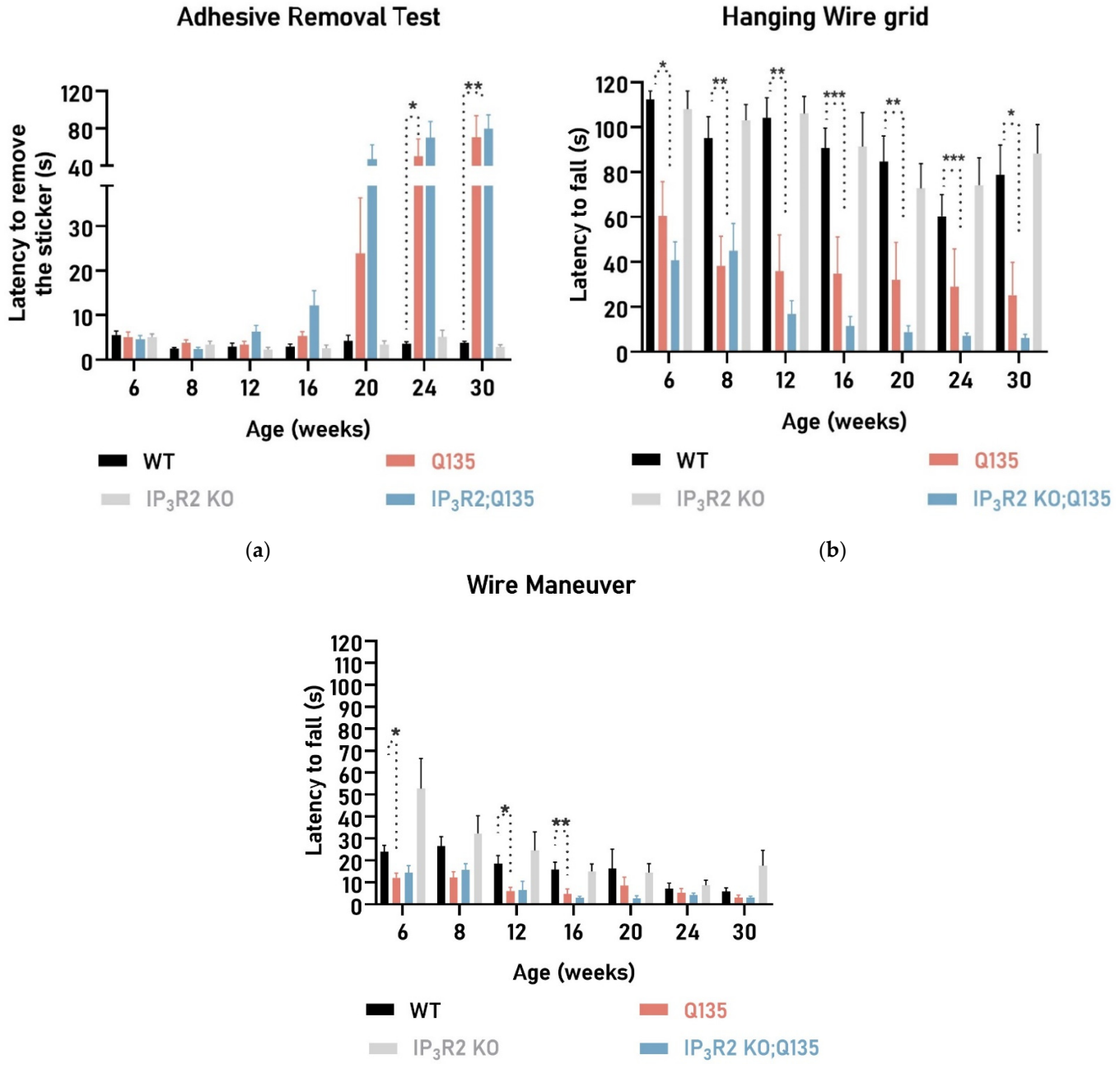

Figure 4. Both the Q135 and IP_3R2 KO; Q135 animals display similarly reduced strength and slower movement initiation. (**a**) In the adhesive removal test, the IP_3R2 KO; Q135 and Q135 mice showed worsening of their performance over time. Evaluation of limb muscular strength assessed by the (**b**) hanging wire grid and the (**c**) wire maneuver test. Assessment of limb strength showed no significant differences between the Q135 and IP_3R2 KO; Q135 mice. Repeated measures ANOVA, one-way ANOVA, and the Kruskal–Wallis test were carried out. All statistical information is included in Appendix A, Table A1. The data are presented as the mean SEM. Asterisks (*) indicate statistical significance between the WT and Q135 mice.The means were considered statistically significant at a *p*-value * $p < 0.05$ and ** $p < 0.01$, *** $p < 0.001$.

3. Discussion

In this work, we explored the contribution of IP_3R2, the main IP_3 receptor responsible for somatic calcium signalling in astrocytes, to the progression of motor symptoms in an

animal model of SCA3. Our results show that ablation of IP_3R2 had no major impact on the motor-related symptoms of a SCA3 animal model, as the IP_3R2 KO; Q135 mice displayed a similar motor phenotype when compared to the CMVMJD135 mouse model.

In the brainstem of the Q135 mice, a key affected brain region, the baseline mRNA levels of *Itpr2* were not altered when compared to the WT mice. The expression levels of the homologous isoform (IP_3R1) were also analyzed to understand whether the deletion of IP_3R2 could affect other IP_3Rs expression changes through a direct compensatory mechanism or through interactions between IP_3R2 and other targets. Our results excluded such compensatory changes.

We confirmed previous observations that Q135 mice display significantly lower body weight gain compared to WT mice and a decline in body weight as the disease progresses. The decline in body weight as the disease progress is most likely associated with the significant atrophy observed in the model [14]. Interestingly, over time, the IP_3R2 KO; Q135 animals displayed a lower body weight when compared to the Q135 mice. This suggests that IP_3R2 can be a modulator of this more "peripheral" aspect of the phenotype. IP_3R2 KO mice have been reported by us [51] and others [47,56] to have a similar body weight when compared to WT mice; however, in the context of SCA3, the absence of IP_3R2 in the IP_3R2 KO; Q135 animals appears to have induced the loss of body weight. This suggests that IP_3R2 could have a detrimental effect on peripheral tissues, and further studies are needed to clarify the functional role of IP_3R2 in SCA3 mice. Studies with calcium imaging and/or experiments of knock-down of IP_3Rs in the peripheral tissues [62,63] could help us to elucidate this point and its relevance for SCA3.

Using tests to evaluate core motor deficits, such as those affecting movement, coordination and balance, our data showed that, unlike what was seen for SCA2 [41] the genetic deletion of IP_3R2 does not alter the disease progression of Q135 animals. Similar results have been described in amyotrophic lateral sclerosis (ALS) mouse models, where the genetic ablation of IP_3R2 showed no impact on disease onset and motor coordination although worsened muscular strength and decreased survival of the $SOD1^{G23A}$ mice [57]. At first glance, the involvement of IP_3R2 in ALS seems controversial, as higher levels of *Itpr2* were shown to be detrimental to the mice and therefore, it would be expected that the ablation of this isoform could have beneficial effects [64]. Contrary to our observations and those made in ALS mice, ablation of this receptor in the ischemic brain as well as in aged mouse brains was shown to be neuroprotective, while reducing behavioral deficits [56]. These observations may indicate a distinct role of astrocytes in different contexts and disease aetiologias. The physiological role of IP_3R2-mediated calcium signalling needs to be studied in different pathological contexts since the absence of IP_3R2 leads to different outcomes according to the context.

We also performed a battery of tests to evaluate muscular strength and movement initiation, a parkinsonism-related manifestation. In these behavioral dimensions, the performance of the IP_3R2 KO; Q135 mice was also indistinguishable from that of the Q135 mice. Overall, these data suggest that the deletion of IP_3R2 had no impact on the motor activity of the IP_3R2 KO; Q135 mice. Despite the likely suppression of global calcium signalling in astrocytes, the IP_3R2 KO mice still have IP_3R2-independent calcium signals through alternative calcium sources and synaptic calcium, such as plasmalemma calcium influx or the mitochondria [27,28,65]. Based on this, it is plausible to question whether the transient calcium signals are robust enough to justify the lack of impact of IP_3R2 deletion in the SCA3 background. Additionally, the possibility of a compensatory mechanism between IP_3R2 and other critical players of calcium signalling exists, including G-protein-coupled receptors. Further studies should be performed to unravel the involvement of other calcium signalling pathways in SCA3 onset and progression, including approaches using pharmacological approaches [63,66–68] or the two-photon excitation microscopy technique [69,70].

Globally, our results demonstrate that SCA3-IP_3R2 double mutants present similar behavior to SCA3 mice, suggesting that the IP_3R2 receptor is not a major modulator of the onset and progression of SCA3 motor symptomatology.

4. Materials and Methods

4.1. Animal Generation and Maintenance

In this study, two mouse models (Mus musculus and strain C57BL/6J) were used to understand the potential involvement of IP_3R2 receptor deletion in SCA3 progression.

The Q135 mice were generated as previously described [14]. The CMVMJD135 mouse model expresses human ATXN3 (cDNA, isoform 3c) under the control of the CMV promoter (ubiquitous expression) at near-endogenous levels [14]. The cDNA variant of the ATXN3 gene carries a repeat tract with the sequence (CAG)2CAAAAGCAGCAA(CAG)129, coding for 135 glutamine [14,71]. The IP_3R2 knock-out (KO) mouse model was supplied by Prof. Alfonso Araque (Minneapolis, MN, USA) [72] under agreement with Prof. Ju Chen (U.C. San Diego, CA, USA) [42]. Initially, the heterozygous *Q135* mice were crossed with homozygous IP_3R2 KO mice, and the following genotypes were obtained: wild-type (WT), heterozygous *Q135* homozygous IP_3R2 KO (IP_3R2 −/−), and heterozygous IP_3R2 KO (IP_3R2 +/−) mice, as well as a double mutant of heterozygous Q135 and heterozygous IP_3R2 KO (IP_3R2 +/−; *Q135*). To generate the experimental groups, the obtained double mutants (IP_3R2 +/−; *Q135*) were crossed with the heterozygous IP_3R2 KO (IP_3R2 +/−), obtaining the following genotypes WT, *Q135*, IP_3R2 −/−, IP_3R2 +/−, and IP_3R2 −/−; *Q135*. To answer our main question, although we performed the behavior analysis with all the obtained genotypes, we focused on the comparison between the WT, *Q135*, and IP_3R2 −/−; *Q135* mice. Male mice were used in this study to increase analysis homogeneity (decrease variance) and to allow for a small number of animals. Because the IP_3R2 heterozygous animals had not been characterized before, we included this group of mice in our analyses. No differences were found in any of the motor-related tests performed when compared to the WT-littermates (see the statistical analyses in Appendix A, Table A1).

The animals were maintained in a conventional animal facility and under standard laboratory conditions, which included an artificial 12 h light/dark cycle, lights on from 8:00 am to 8:00 pm, an ambient temperature of 21 ± 1 °C, and a relative humidity of 50–60%. The mice were given a standard 4RF25 diet during the gestation and postnatal periods and a 4RF21 diet after weaning (3 weeks of age; Mucedola SRL, Settimo Milanese, Italia) as well as water ad libitum. During weaning, the mice were housed in groups of six animals in filter topped polysulfone cages 267 × 207 × 140 mm (370 cm^2 floor area) (Tecniplast, Buguggiate, VA, Italy) using corncob bedding (Scobis Due, Mucedola SRL). Environmental enrichment consisted of soft tissue paper and shredded paper to stimulate the natural behavior of nesting.

4.2. Molecular Analysis: Macrodissection, RNA Isolation, cDNA Synthesis, and Real-Time Quantitative PCR Analysis

In order to assess the transcription levels of the *Itpr2* gene, relative mRNA levels of the *Itpr2* gene were quantified by real-time quantitative reverse-transcriptase polymerase chain reaction analysis (qRT-PCR). For this, the WT (n = 8), Q135 (n = 9), IP_3R2 KO (n = 3), and IP_3R2 KO; Q135 (n = 5) animals were euthanized, their brains were harvested, and their brainstems (a key affected region in SCA3) were macrodissected.

Total RNA was isolated from the tissues using TRIZOL (Invitrogen, Waltham, MA, USA) according to the manufacturer's protocol. First-strand complementary DNA (cDNA), synthesized using the iScript™ cDNA Synthesis Kit (Bio-Rad, Hercules, FL, USA), was amplified by qRT-PCR according to the guidelines (Bio-Rad, Hercules, FL, USA).

The primers used in this study (Table 1) were designed using PRIMER-BLAST (NCBI, Bethesda, Rockville, ML, USA; http://www.ncbi.nlm.nih.gov/tools/primer-blast/, accessed on 1 June 2019). Quantification was performed using the Fast Real-Time PCR System (Applied Biosystems, Waltham, MA, USA). The housekeeping beta-2-microglobulin (*B2m*)

gene was used as an internal control. The relative gene expression was determined using the $2^{-\Delta\Delta Ct}$ relative quantification method and represented as fold change normalized to the mean of the relative expression of the wild-type mice. The PCR cycling conditions used were denaturation at 95 °C for 30 s, 30 cycles at 95 °C for 5 s, annealing at 60 °C for 30 s, plus an extension at 65 °C for 5 s, and a final extension at 95 °C for 5 s.

Table 1. Primer sequences used for the analysis of gene expression (qRT-PCR).

Gene	Primer Sequence	
Itpr1	Foward 5′-CTCTGTATGCGGAGGGATCTAC-3′	Reverse 5′-GCGGAGTATCGATTCATAGGAC-3′
Itpr2	Foward 5′-CTTCCTCTACATTGGGGACATC-3′	Reverse 5′-GGCAGAGTATCGATTCATAGGG-3′
B2m	Foward 5′-CCTTCAGCAAGGACTGGTCT-3′	Reverse 5′-TCTCGATCCCAGTAGACGGT-3′

The primers were designed using PRIMER-BLAST (NCBI, http://www.ncbi.nlm.nih.gov/tools/primer-blast/, accessed on 1 June 2019).

4.3. Behavior Analysis

Behavioral tests were performed during the diurnal period, and the animals were tested at 6, 8, 12, 16, 20, 24, and 30 weeks of age. Body weight was registered at all time points analyzed. Motor behavior was assessed using the balance beam walk test (12-mm square and 11-mm round beams) and the motor swimming test. Furthermore, movement initiation was evaluated with the adhesive removal test, and muscular strength parameters were assessed using the hanging wire grid and the wire maneuver tests. The behavioral tests are briefly explained below:

4.3.1. Motor Swimming Test

The motor swimming test was used to evaluate voluntary locomotion, by taking advantage of the survival instinct of mice in water environments [73]. Each mouse was gently placed at one end of a 100 cm clear acrylic tank filled with water (15 cm depth), maintained at 23 °C ± 1 °C using a thermostat, and trained for 2 consecutive days (3 trials/animal), to reach a visible black platform at the opposite end. During the following 3 days, the animals were tested, and the time that it took each mouse to cross the water tank was recorded (2 trials/mouse) [73]. The tank was labelled with a blue line to mark the starting position, and the mice swam a distance of 60 cm to complete the trial.

4.3.2. Beam Balance Test

Balance and fine motor coordination were evaluated by the latency of each mouse to traverse different diameters and shape beams to reach a safe platform [73]. The beams consisted of long strips of PVC (1 m) with a 12 mm square cross-section or 11 mm round diameter. The beams were placed horizontally, 50 cm above the bench surface, protected with soft sponges to protect the mice from falls, with one end mounted on a narrow support and the other end attached to an enclosed dark box (20 cm square), into which the mouse could escape. The mice were trained for 3 consecutive days on the 12 mm-squared beam (3 trials/animal), and on the fourth day, the animals were tested on both beams (2 trials/animal). The time each mouse took to cross the beams was recorded and discounted if the animal stopped in the beam. A failed trial was considered when an animal fell or turned around on the beam. Each animal had the opportunity to fail twice on each beam [73]. Because the Q135 mice showed a worsening of the phenotype at 16 weeks of age, which affects the ability to perform the task causing them to fall off the beams very frequently, we analyzed the data by attributing performance scores to the animals as follows: 0—performed 2 trials, 1—performed 1 trial, and 2—performed 0 trials, meaning that it cannot walk on the beam.

4.3.3. Adhesive Removal Test

In the adhesive removal test, the experimenter gently placed a round adhesive (8 mm diameter) on the nose of the mouse and transferred the animal to a cage. The time the animal took to remove the adhesive was registered [61,74].

4.3.4. Hanging Wire Grid Test

In the hanging wire grid test, the mice were placed on top of a metallic horizontal grid and inverted 180° towards the surface of the bench (protected with soft sponges to protect the mice from falls). With this test, the latency for the mice to fall off the metal grid was evaluated. The maximum time of the test allowed was 120 s [73,75].

4.3.5. Wire Maneuver Test

The mice were picked up by their tails, and their forelimbs were placed to a fixed wire, underneath of which soft sponges were placed to protect them from falls. This test is based on the latency to fall off the metal wire and the maximum allowed time of the test was 120 s [75].

4.4. Statistical Analysis

The G*Power 3.1.9.2 software was used to calculate the required sample size, based on a power of 0.8 (obtained from previous data) [76] and a significance level of 0.05 was used for all statistical tests.

All statistical analyses were performed using SPSS 22.0. The statistical analysis of the behavior tests was performed including all the genotypes under study (including IP_3R2 −/+); however, the results presented in this study were divided into two groups to simplify the visualizations of the key comparisons as well as to answer the study's main question. Behavioral data were analyzed by a repeated-measures ANOVA when the variables were continuous or presented a normal distribution. Values that deviated more than 1.5 interquartile ranges from the mean were considered outliers and excluded from further analyses. The assumption of normality was assessed by qualitative analysis of Q-Q plots and frequency distributions (z-score of skewness and kurtosis) as well as by the Kolmogorov–Smirnov and Shapiro–Wilk tests. The assumption of homogeneity of variances was evaluated by Levene's test. Regarding repeated measurements, sphericity was tested using Mauchly's test and assumed for all tested variables. For the comparison of means between 5 groups, one-way analysis of variance (ANOVA) was used, followed by Tukey HSD or Dunnett T3's test (when data passed on the assumption of homogeneity of variances or when the populations variances were not equal, respectively).

Regarding non-normally distributed data and/or for the comparison of medians of discrete variables across time points, a Friedman's ANOVA was carried out, with pairwise comparisons through the Kruskal–Wallis statistical test.

Effect size measurements are reported for all analyses (Cohen's d for *t*-tests and eta partial square—n_p^2 for ANOVAs). GraphPad Prism 8 was used to create graphs. All figures were created using PowerPoint (version 2305, Microsoft 365 MSO). All statistical information is reported in Appendix A.

5. Conclusions

Although behavioral evaluation of the IP_3R2 KO; Q135 mice revealed the presence of several phenotypic manifestations seen in the CMVMJD135 mouse model, that gradually appear and progress during the mice lifespan, both the Q135 and IP_3R2 KO; Q135 mice displayed equivalent balance and motor coordination deficits, loss of limb strength, and abnormal gait. Thus, the phenotypical abnormalities induced by mutant human ATXN3 were not altered by the absence of IP_3R2, the phenotype manifested by the IP_3R2 KO; Q135 mice which is attributable to the Q135 phenotype already well-described in the literatu [14,71,76–84]. This suggests that IP_3R2 is not a major modulator of disease severity in SCA3.

Author Contributions: Conceptualization, D.C.-G., P.M. and S.D.-S.; data curation, D.C.-G. and A.C.V.-F.; formal analysis, D.C.-G.; funding acquisition, P.M.; investigation, D.C.-G., D.M.-F., J.S.C., A.N.-C., S.G.-G. and J.F.V.; methodology, D.C.-G., D.M.-F., J.S.C., A.N.-C., S.G.-G., J.F.V., J.F.O. and A.T.-C.; project administration, P.M. and S.D.-S.; resources, J.F.O., A.T.-C. and P.M.; supervision, P.M. and S.D.-S.; validation, P.M. and S.D.-S.; visualization, D.C.-G. and A.C.V.-F.; writing—original draft, D.C.-G.; writing—review and editing, D.C.-G., P.M. and S.D.-S. All authors have read and agreed to the published version of the manuscript.

Funding: This work has been funded by National funds, through the Foundation for Science and Technology (FCT)—project UIDB/50026/2020 and UIDP/50026/2020, PTDC/NEUNMC/3648/2014 and COMPETE-FEDER (POCI-01-0145-FEDER-016818); fellowships to DCG (2021.08121.BD), DMF (SFRH/BD/147947/2019), JSC (SFRH/BD/140624/2018), ANC (SFRH/BPD/118779/2016), AVF (UMINHO/BIL-CNCG/2022/11), SGG (SFRH/BD/101298/2014), and JFV (2020.05109.BD); FCT Scientific Employment Stimulus (CEEC)—Individual Call position to SDS (CEECIND/00685/2020); grants from the Bial Foundation (037/18) and "the la Caixa" Foundation (LCF/PR/HR21/52410024) to JFO; and by the projects NORTE-01-0145-FEDER-000013 and NORTE-01-0145-FEDER-000023, supported by the Norte Portugal Regional Operational Programme (NORTE 2020), under the PORTUGAL 2020 Partnership Agreement, through the European Regional Development Fund (ERDF). It was also supported by grants from the ICVS Scientific Microscopy Platform, a member of the national infrastructure PPBI—Portuguese Platform of Bioimaging (PPBI-POCI-01-0145-FEDER-022122 and national funds through the Foundation for Science and Technology (FCT).

Institutional Review Board Statement: The animal study protocol was approved by the Animal Ethics Committee of the Life and Health Sciences Research Institute, University of Minho (Braga, Portugal) and by the legal entity Direção Geral da Alimentação e Veterinária (DGAV; reference of the license 020317). The animal experimentation and reporting were designed and conducted in adherence with ARRIVE 2.0 guidelines (Animal Research: Reporting In Vivo Experiments). The animal facilities and the people directly involved in the animal experiments are certified by the Portuguese regulatory entity—Direcção Geral de Alimentação e Veterinária (DGAV, license number 012668).

Data Availability Statement: The datasets used and/or analyzed during the current study are available from the corresponding author upon reasonable request.

Acknowledgments: The authors are grateful to Alfonso Araque and Ju Chen for sharing the mice line.

Conflicts of Interest: The authors declare no conflict of interest.

Abbreviations

AD: Alzheimer's disease; ALS: amyotrophic lateral sclerosis; ATXN3: ataxin-3 protein; CNS: central nervous system; ER: endoplasmic reticulum; Het: heterozygous; HD: Huntington's disease; IP_3: inositol 1,4,5-trisphosphate molecules; IP_3Rs: inositol 1,4,5-trisphosphate receptors; IP_3R2 KO: inositol 1,4,5-trisphosphate receptor type 2 knock-out; IP_3R2 (−/−): inositol 1,4,5-trisphosphate receptor type 2 knock-out; IP_3R2 HET: inositol 1,4,5-trisphosphate receptor type 2 heterozygous; IP_3R2 (+/−): inositol 1,4,5-trisphosphate receptor type 2 heterozygous; KO: knockout; PD: Parkinson's disease; qRT-PCR: quantitative real-time polymerase chain reaction; RT: room temperature; SCA1: spinocerebellar ataxia type 1; SCA2: spinocerebellar ataxia type 2; SCA3: spinocerebellar ataxia type 3; SCAs: spinocerebellar ataxias; SEM: standard error of the mean; WT: wild-type.

Appendix A

Table A1. Statistical information of behavioral characterization.

Itpr1	**One-way ANOVA, with Tukey HSD comparisons** F (3,24) = 0.399, $p = 0.755$ WT vs. Q135 $p = 0.990$ WT vs. IP_3R2 KO $p = 0.999$ Q135 vs. IP_3R2; Q135 $p = 0.706$	***n*** (WT) = 8 ***n*** (Q135) = 9 ***n*** (IP_3R2 KO) = 3 ***n*** (IP_3R2; Q135) = 5

Table A1. *Cont.*

Itpr2	One-way ANOVA, with Dunnett T3 comparisons F (3,24) = 7.888, $p = 0.001$ WT vs. Q135 $p = 1.000$ WT vs. IP_3R2 KO $p = 0.027$ Q135 vs. IP_3R2; Q135 $p < 0.001$	n (WT) = 8 n (Q135) = 9 n (IP_3R2 KO) = 3 n (IP_3R2; Q135) = 5
CAG number	Independent *t*-test t (15,10) = −0.080, $p = 0.937$	n (Q135) = 6 n (IP_3R2; Q135) = 11
Body Weight	Repeated Measures ANOVA, with Tukey HSD comparisons Within-subjects effect | F (10,82) = 12.596, $p < 0.001$ $n_p^2 = 0.604$ Between-subjects effect | F (4,33) = 18.178, $p < 0.001$ $n_p^2 = 0.688$ WT vs. Q135 $p = 0.043$ WT vs. IP_3R2 KO $p = 0.960$ WT vs. IP_3R2 HET $p = 0.991$ Q135 vs. IP_3R2; Q135 $p = 0.008$	n (WT) = 12 n (Q135) = 9 n (IP_3R2 KO) = 10 n (IP_3R2; HET) = 6 n (IP_3R2; Q135) = 12
	One-way ANOVA, with Tukey HSD comparisons Week 12 F (4,48) = 11.075, $p \leq 0.001$ WT vs. Q135 $p = 0.005$ WT vs. IP_3R2 KO $p = 0.734$ WT vs. IP_3R2 HET $p = 0.790$ Q135 vs. IP_3R2; Q135 $p = 0.342$ Week 16 F (4,48) = 12.052, $p \leq 0.001$ WT vs. Q135 $p = 0.018$ WT vs. IP_3R2 KO $p = 1.000$ WT vs. IP_3R2 HET $p = 0.986$ Q135 vs. IP_3R2; Q135 $p = 0.426$ Week 20 F (4,47) = 28.619, $p \leq 0.001$ WT vs. Q135 $p < 0.001$ WT vs. IP_3R2 KO $p = 0.950$ WT vs. IP_3R2 HET $p = 0.996$ Q135 vs. IP_3R2; Q135 $p = 0.133$ Week 24 F (4,47) = 34.103, $p \leq 0.001$ WT vs. Q135 $p < 0.001$ WT vs. IP_3R2 KO $p = 0.894$ WT vs. IP_3R2 HET $p = 1.000$ Q135 vs. IP_3R2; Q135 $p = 0.085$ Week 30 F (4,41) = 30.343, $p \leq 0.001$ WT vs. Q135 $p < 0.001$ WT vs. IP_3R2 KO $p = 1.000$ WT vs. IP_3R2 HET $p = 1.000$ Q135 vs. IP_3R2; Q135 $p = 0.076$	

Table A1. *Cont.*

Motor Swimming test	Repeated Measures ANOVA, with Tukey HSD comparisons Within-subjects effect | F (15,116) = 5.660, $p < 0.001$ $n_p^2 = 0.422$ Between-subjects effect | F (4,31) = 10.592, $p < 0.001$ $n_p^2 = 0.577$ WT vs. Q135 $p = 0.003$ WT vs. IP_3R2 KO $p = 0.960$ WT vs. IP_3R2 HET $p = 0.982$ Q135 vs. IP_3R2; Q135 $p = 0.994$	
	One-way ANOVA, with Tukey HSD comparisons Week 12 F (4,48) = 8.573, $p \leq 0.001$ WT vs. Q135 $p = 0.019$ WT vs. IP_3R2 KO $p = 0.669$ WT vs. IP_3R2 HET $p = 0.102$ Q135 vs. IP_3R2; Q135 $p = 0.307$ Week 16 F (4,48) = 6.000, $p = 0.001$ WT vs. Q135 $p = 0.027$ WT vs. IP_3R2 KO $p = 0.999$ WT vs. IP_3R2 HET $p = 0.992$ Q135 vs. IP_3R2; Q135 $p = 1.000$ Week 20 F (4,47) = 11.852, $p \leq 0.001$ WT vs. Q135 $p = 0.002$ WT vs. IP_3R2 KO $p = 0.997$ WT vs. IP_3R2 HET $p = 0.991$ Q135 vs. IP_3R2; Q135 $p = 0.999$ Week 24 F (4,45) = 18,597, $p \leq 0.001$ WT vs. Q135 $p < 0.001$ WT vs. IP_3R2 KO $p = 0.996$ WT vs. IP_3R2 HET $p = 0.600$ Q135 vs. IP_3R2; Q135 $p = 1.000$ Week 30 F (4,39) = 13,979, $p \leq 0.001$ WT vs. Q135 $p < 0.001$ WT vs. IP_3R2 KO $p = 0.999$ WT vs. IP_3R2 HET $p = 1.000$ Q135 vs. IP_3R2; Q135 $p = 0.988$	*n* (WT) = 12 *n* (Q135) = 9 *n* (IP_3R2 KO) = 10 *n* (IP_3R2; HET) = 6 *n* (IP_3R2; Q135) = 12

Table A1. *Cont.*

Beam Walking Test 12 mm square (6–20 week)	Repeated Measures ANOVA, with Tukey HSD comparisons Within-subjects effect | F (10,67) = 4.901, $p < 0.001$ $n_p^2 = 0.403$ Between-subjects effect | F (4,29) = 13.460, $p < 0.001$ $n_p^2 = 0.650$ WT vs. Q135 $p = 0.028$ WT vs. IP$_3$R2 KO $p = 0.784$ WT vs. IP$_3$R2 HET $p = 0.986$ Q135 vs. IP$_3$R2; Q135 $p = 0.193$	*n* (WT) = 12 *n* (Q135) = 9 *n* (IP$_3$R2 KO) = 10 *n* (IP$_3$R2; HET) = 6 *n* (IP$_3$R2; Q135) = 12
	One-way ANOVA, with Tukey HSD comparisons Week 12 F (4,44) = 11.955, $p < 0.001$ WT vs. Q135 $p = 0.015$ WT vs. IP$_3$R2 KO $p = 1.000$ WT vs. IP$_3$R2 HET $p = 0.986$ Q135 vs. IP$_3$R2; Q135 $p = 0.405$ Week 16 F (4,43) = 20.203, $p < 0.001$ WT vs. Q135 $p = 0.063$ WT vs. IP$_3$R2 KO $p = 0.999$ WT vs. IP$_3$R2 HET $p = 0.999$ Q135 vs. IP$_3$R2; Q135 $p = 0.008$ Week 20 F (4,38) = 25.265, $p < 0.001$ WT vs. Q135 $p < 0.001$ WT vs. IP$_3$R2 KO $p = 0.940$ WT vs. IP$_3$R2 HET $p = 0.971$ Q135 vs. IP$_3$R2; Q135 $p = 1.000$	
Beam Walking Test—12 mm square 24–30 week (Score)	Kruskal–Wallis test 24 week $\chi^w 2$ (4,47) = 28.174 $p < 0.001$ $n_p^2 = 0.585$ WT vs. Q135 $p < 0.001$ WT vs. IP$_3$R2 KO $p = 1.000$ WT vs. IP$_3$R2 HET $p = 1.000$ Q135 vs. IP$_3$R2; Q135 $p = 0.972$ 30 week $\chi^w 2$ (4,40) = 27.513 $p < 0.001$ $n_p^2 = 0.681$ WT vs. Q135 $p = 0.002$ WT vs. IP$_3$R2 KO $p = 1.000$ WT vs. IP$_3$R2 HET $p = 1.000$ Q135 vs. IP$_3$R2; Q135 $p = 0.743$	*n* (WT) = 11 *n* (Q135) = 9 *n* (IP$_3$R2 KO) = 10 *n* (IP$_3$R2; HET) = 6 *n* (IP$_3$R2; Q135) = 11

Table A1. *Cont.*

Beam Walking Test—11 mm circle 6–30 week (Score)	Kruskal–Wallis test 8 week χ^w2 (4,46) = 16.832 p = 0.002 n_p^2 = 0.329 WT vs. Q135 p = 0.006 WT vs. IP_3R2 KO p = 1.000 WT vs. IP_3R2 HET p = 1.000 Q135 vs. IP_3R2; Q135 p = 0.959 12 week χ^w2 (4,49) = 29.833 p < 0.001 n_p^2 = 0.596 WT vs. Q135 p = 0.002 WT vs. IP_3R2 KO p = 1.000 WT vs. IP_3R2 HET p = 0.460 Q135 vs. IP_3R2; Q135 p = 0.377 16 week χ^w2 (4,49) = 36.432 p < 0.001 n_p^2 = 0.743 WT vs. Q135 p < 0.001 WT vs. IP_3R2 KO p = 1.000 WT vs. IP_3R2 HET p = 1.000 Q135 vs. IP_3R2; Q135 p = 0.560 20 week χ^w2 (4,48) = 29.218 p < 0.001 n_p^2 = 0.596 WT vs. Q135 p = 0.002 WT vs. IP_3R2 KO p = 0.666 WT vs. IP_3R2 HET p = 0.710 Q135 vs. IP_3R2; Q135 p = 0.907 24 week χ^w2 (4,47) = 38.818 p < 0.001 n_p^2 = 0.833 WT vs. Q135 p < 0.001 WT vs. IP_3R2 KO p = 1.000 WT vs. IP_3R2 HET p = 1.000 Q135 vs. IP_3R2; Q135 p = 0.387 30 week χ^w2 (4,41) = 26.704 p < 0.001 n_p^2 = 0.641 WT vs. Q135 p = 0.004 WT vs. IP_3R2 KO p = 1.000 WT vs. IP_3R2 HET p = 0.517 Q135 vs. IP_3R2; Q135 p = 0.440	*n* (WT) = 12 *n* (Q135) = 9 *n* (IP_3R2 KO) = 10 *n* (IP_3R2; HET) = 6 *n* (IP_3R2; Q135) = 12

Table A1. *Cont.*

Adhesive Removal	Repeated Measures ANOVA, with Tukey HSD comparisons Within-subjects effect | F (10,80) = 4.439, $p < 0.001$ $n_p^2 = 0.350$ Between-subjects effect | F (4,33) = 7.379, $p < 0.001$ $n_p^2 = 0.472$ WT vs. Q135 $p = 0.097$ WT vs. IP_3R2 KO $p = 1.000$ WT vs. IP_3R2 HET $p = 1.000$ Q135 vs. IP_3R2; Q135 $p = 0.788$	*n* (WT) = 12 *n* (Q135) = 9 *n* (IP_3R2;KO) = 10 *n* (IP_3R2; HET) = 6 *n* (IP_3R2;Q135) = 12
	One-way ANOVA, with Tukey HSD comparisons Week 24 F (4,47) = 7.509, $p < 0.001$ WT vs. Q135 $p = 0.044$ WT vs. IP_3R2 KO $p = 1.000$ WT vs. IP_3R2 HET $p = 1.000$ Q135 vs. IP_3R2; Q135 $p = 0.743$ Week 30 F (4,41) = 10.509, $p < 0.001$ WT vs. Q135 $p = 0.006$ WT vs. IP_3R2 KO $p = 1.000$ WT vs. IP_3R2 HET $p = 1.000$ Q135 vs. IP_3R2; Q135 $p = 0.983$	

Table A1. *Cont.*

Hanging Wire Grid	Kruskal–Wallis test 6 week χ^w2 (4,49) = 26.873 $p < 0.001$ $n_p^2 = 0.531$ WT vs. Q135 $p = 0.018$ WT vs. IP_3R2 KO $p = 0.855$ WT vs. IP_3R2 HET $p = 0.637$ Q135 vs. IP_3R2; Q135 $p = 0.199$ 8 week χ^w2 (4,46) = 17,550 $p = 0.002$ $n_p^2 = 0.346$ WT vs. Q135 $p = 0.006$ WT vs. IP_3R2 KO $p = 0.700$ WT vs. IP_3R2 HET $p = 0.761$ Q135 vs. IP_3R2; Q135 $p = 0.871$ 12 week χ^w2 (4,49) = 26.969 $p < 0.001$ $n_p^2 = 0.533$ WT vs. Q135 $p = 0.009$ WT vs. IP_3R2 KO $p = 0.678$ WT vs. IP_3R2 HET $p = 0.718$ Q135 vs. IP_3R2; Q135 $p = 0.391$ 16 week χ^w2 (4,49) = 23.184 $p < 0.001$ $n_p^2 = 0.449$ WT vs. Q135 $p = 0.031$ WT vs. IP_3R2 KO $p = 0.799$ WT vs. IP_3R2 HET $p = 0.813$ Q135 vs. IP_3R2; Q135 $p = 0.201$ 20 week χ^w2 (4,48) = 25.962 $p < 0.001$ $n_p^2 = 0.522$ WT vs. Q135 $p = 0.006$ WT vs. IP_3R2 KO $p = 0.675$ WT vs. IP_3R2 HET $p = 0.920$ Q135 vs. IP_3R2; Q135 $p = 0.282$ 24 week χ^w2 (4,48) = 24.298 $p < 0.001$ $n_p^2 = 0.484$ WT vs. Q135 $p = 0.008$ WT vs. IP_3R2 KO $p = 0.587$ WT vs. IP_3R2 HET $p = 0.459$ Q135 vs. IP_3R2; Q135 $p = 0.719$ 30 week χ^w2 (4,42) = 25.541 $p < 0.001$ $n_p^2 = 0.593$ WT vs. Q135 $p = 0.014$ WT vs. IP_3R2 KO $p = 0.699$ WT vs. IP_3R2 HET $p = 0.883$ Q135 vs. IP_3R2; Q135 $p = 0.444$	*n* (WT) = 12 *n* (Q135) = 9 *n* (IP_3R2 KO) = 10 *n* (IP_3R2; HET) = 6 *n* (IP_3R2; Q135) = 12

Table A1. *Cont.*

Wire Manouver	Kruskal–Wallis test 6 week χ^w2 (4,49) = 19.771 p = 0.001 $n_p{}^2$ = 0.373 WT vs. Q135 p = 0.011 WT vs. IP_3R2 KO p = 0.210 WT vs. IP_3R2 HET p = 0.560 Q135 vs. IP_3R2; Q135 p = 0.549	
	12 week χ^w2 (4,49) = 20.302 p < 0.001 $n_p{}^2$ = 0.384 WT vs. Q135 p = 0.020 WT vs. IP_3R2 KO p = 0.976 WT vs. IP_3R2 HET p = 0.616 Q135 vs. IP_3R2; Q135 p = 0.442	n (WT) = 12 n (Q135) = 9 n (IP_3R2 KO) = 10 n (IP_3R2; HET) = 6 n (IP_3R2; Q135) = 12
	16 week χ^w2 (4,49) = 20.585 p < 0.001 $n_p{}^2$ = 0.391 WT vs. Q135 p = 0.004 WT vs. IP_3R2 KO p = 0.699 WT vs. IP_3R2 HET p = 0.568 Q135 vs. IP_3R2; Q135 p = 0.944	

References

1. Coutinho, P.; Andrade, C. Autosomal dominant system degeneration in Portuguese families of the Azores Islands. A new genetic disorder involving cerebellar, pyramidal, extrapyramidal and spinal cord motor functions. *Neurology* **1978**, *28*, 703–709. [CrossRef]
2. Lima, L.; Coutinho, P. Clinical criteria for diagnosis of Machado-Joseph disease: Report of a non-Azorena Portuguese family. *Neurology* **1980**, *30*, 319–322. [CrossRef] [PubMed]
3. Kawaguchi, Y.; Okamoto, T.; Taniwaki, M.; Aizawa, M.; Inoue, M.; Katayama, S.; Kawakami, H.; Nakamura, S.; Nishimura, M.; Akiguchi, I.; et al. CAG expansions in a novel gene for Machado-Joseph disease at chromosome 14q32.1. *Nat. Genet.* **1994**, *8*, 221–228. [CrossRef] [PubMed]
4. Ichikawa, Y.; Goto, J.; Hattori, M.; Toyoda, A.; Ishii, K.; Jeong, S.Y.; Hashida, H.; Masuda, N.; Ogata, K.; Kasai, F.; et al. The genomic structure and expression of MJD, the Machado-Joseph disease gene. *J. Hum. Genet.* **2001**, *46*, 413–422. [CrossRef] [PubMed]
5. Rosenberg, R.N. Machado-Joseph disease: An autosomal dominant motor system degeneration. *Mov. Disord.* **1992**, *7*, 193–203. [CrossRef]
6. Dürr, A.; Stevanin, G.; Cancel, G.; Duyckaerts, C.; Abbas, N.; Didierjean, O.; Chneiweiss, H.; Benomar, A.; Lyon-Caen, O.; Julien, J.; et al. Spinocerebellar ataxia 3 and Machado-Joseph disease: Clinical, molecular, and neuropathological features. *Ann. Neurol.* **1996**, *39*, 490–499. [CrossRef]
7. Riess, O.; Rüb, U.; Pastore, A.; Bauer, P.; Schöls, L. SCA3: Neurological features, pathogenesis and animal models. *Cerebellum* **2008**, *7*, 125–137. [CrossRef]
8. Horimoto, Y.; Matsumoto, M.; Akatsu, H.; Kojima, A.; Yoshida, M.; Nokura, K.; Yuasa, H.; Katada, E.; Yamamoto, T.; Kosaka, K.; et al. Longitudinal study on MRI intensity changes of Machado-Joseph disease: Correlation between MRI findings and neuropathological changes. *J. Neurol.* **2011**, *258*, 1657–1664. [CrossRef]
9. Coutinho, P.; Guimarães, A.; Scaravilli, F. The pathology of Machado-Joseph disease. *Acta Neuropathol.* **1982**, *58*, 48–54. [CrossRef]
10. Rüb, U.; de Vos, R.A.I.; Schultz, C.; Brunt, E.R.; Paulson, H.; Braak, H. Spinocerebellar ataxia type 3 (Machado-Joseph disease): Severe destruction of the lateral reticular nucleus. *Brain J. Neurol.* **2002**, *125 Pt 9*, 2115–2124. [CrossRef]
11. Rüb, U.; Gierga, K.; Brunt, E.R.; de Vos, R.A.I.; Bauer, M.; Schöls, L.; Bürk, K.; Auburger, G.; Bohl, J.; Schultz, C.; et al. Spinocerebellar ataxias types 2 and 3: Degeneration of the pre-cerebellar nuclei isolates the three phylogenetically defined regions of the cerebellum. *J. Neural Transm.* **2005**, *112*, 1523–1545. [CrossRef] [PubMed]
12. Switonski, P.M.; Szlachcic, W.J.; Krzyzosiak, W.J.; Figiel, M. A new humanized ataxin-3 knock-in mouse model combines the genetic features, pathogenesis of neurons and glia and late disease onset of SCA3/MJD. *Neurobiol. Dis.* **2015**, *73*, 174–188. [CrossRef] [PubMed]
13. Scherzed, W.; Brunt, E.R.; Heinsen, H.; de Vos, R.A.; Seidel, K.; Bürk, K.; Schöls, L.; Auburger, G.; Del Turco, D.; Deller, T.; et al. Pathoanatomy of cerebellar degeneration in spinocerebellar ataxia type 2 (SCA2) and type 3 (SCA3). *Cerebellum* **2012**, *11*, 749–760. [CrossRef] [PubMed]
14. Silva-Fernandes, A.; Duarte-Silva, S.; Neves-Carvalho, A.; Amorim, M.; Soares-Cunha, C.; Oliveira, P.; Thirstrup, K.; Teixeira-Castro, A.; Maciel, P. Chronic treatment with 17-DMAG improves balance and coordination in a new mouse model of Machado-Joseph disease. *Neurotherapeutics* **2014**, *11*, 433–449. [CrossRef]

15. Li, Y.X.; Sibon, O.C.M.; Dijkers, P.F. Inhibition of NF-κB in astrocytes is sufficient to delay neurodegeneration induced by proteotoxicity in neurons. *J. Neuroinflamm.* **2018**, *15*, 261. [CrossRef]
16. Kim, D.-H.; Kim, R.; Lee, J.-Y.; Lee, K.-M. Clinical, Imaging, and Laboratory Markers of Premanifest Spinocerebellar Ataxia 1, 2, 3, and 6: A Systematic Review. *J. Clin. Neurol.* **2021**, *17*, 187–199. [CrossRef]
17. da Silva Carvalho, G.; Saute, J.A.M.; Haas, C.B.; Torrez, V.R.; Brochier, A.W.; Souza, G.N.; Furtado, G.V.; Gheno, T.; Russo, A.; Monte, T.L.; et al. Cytokines in Machado Joseph Disease/Spinocerebellar Ataxia 3. *Cerebellum* **2016**, *15*, 518–525. [CrossRef]
18. Parpura, V.; Verkhratsky, A. Homeostatic function of astrocytes: Ca^{2+} and Na^{+} signalling. *Transl. Neurosci.* **2012**, *3*, 334–344. [CrossRef]
19. Ben Haim, L.; Rowitch, D.H. Functional diversity of astrocytes in neural circuit regulation. *Nat. Rev. Neurosci.* **2017**, *18*, 31–41. [CrossRef]
20. Mederos, S.; González-Arias, C.; Perea, G. Astrocyte–Neuron Networks: A Multilane Highway of Signaling for Homeostatic Brain Function. *Front. Synaptic Neurosci.* **2018**, *10*, 45. [CrossRef]
21. Verkhratsky, A.; Nedergaard, M. Physiology of Astroglia. *Physiol. Rev.* **2018**, *98*, 239–389. [CrossRef]
22. Araque, A.; Parpura, V.; Sanzgiri, R.P.; Haydon, P.G. Tripartite synapses: Glia, the unacknowledged partner. *Trends Neurosci.* **1999**, *22*, 208–215. [CrossRef]
23. Araque, A.; Carmignoto, G.; Haydon, P.G.; Oliet, S.H.R.; Robitaille, R.; Volterra, A. Gliotransmitters Travel in Time and Space. *Neuron* **2014**, *81*, 728–739. [CrossRef] [PubMed]
24. Guerra-Gomes, S.; Sousa, N.; Pinto, L.; Oliveira, J.F. Functional Roles of Astrocyte Calcium Elevations: From Synapses to Behavior. *Front. Cell. Neurosci.* **2017**, *11*, 427. [CrossRef] [PubMed]
25. Agulhon, C.; Petravicz, J.; McMullen, A.B.; Sweger, E.J.; Minton, S.K.; Taves, S.R.; Casper, K.B.; Fiacco, T.A.; McCarthy, K.D. What Is the Role of Astrocyte Calcium in Neurophysiology? *Neuron* **2008**, *59*, 932–946. [CrossRef]
26. Matyash, M.; Matyash, V.; Nolte, C.; Sorrentino, V.; Kettenmann, H. Requirement of functional ryanodine receptor type 3 for astrocyte migration. *FASEB J.* **2002**, *16*, 84–86. [CrossRef]
27. Agarwal, A.; Wu, P.-H.; Hughes, E.G.; Fukaya, M.; Tischfield, M.A.; Langseth, A.J.; Wirtz, D.; Bergles, D.E. Transient Opening of the Mitochondrial Permeability Transition Pore Induces Microdomain Calcium Transients in Astrocyte Processes. *Neuron* **2017**, *93*, 587–605.e7. [CrossRef] [PubMed]
28. Okubo, Y.; Kanemaru, K.; Suzuki, J.; Kobayashi, K.; Hirose, K.; Iino, M. Inositol 1,4,5-trisphosphate receptor type 2-independent Ca^{2+} release from the endoplasmic reticulum in astrocytes. *Glia* **2019**, *67*, 113–124. [CrossRef] [PubMed]
29. Mikoshiba, K. IP3 receptor/Ca^{2+} channel: From discovery to new signaling concepts. *J. Neurochem.* **2007**, *102*, 1426–1446. [CrossRef]
30. Furuichi, T.; Kohda, K.; Miyawaki, A.; Mikoshiba, K. Intracellular channels. *Curr. Opin. Neurobiol.* **1994**, *4*, 294–303. [CrossRef]
31. Michikawa, T.; Miyawaki, A.; Furuichi, T.; Mikoshiba, K. Inositol 1,4,5-trisphosphate receptors and calcium signaling. *Crit. Rev. Neurobiol.* **1996**, *10*, 39–55. [CrossRef] [PubMed]
32. Sharp, A.H.; Nucifora, F.C.; Blondel, O.; Sheppard, C.A.; Zhang, C.; Snyder, S.H.; Russell, J.T.; Ryugo, D.K.; Ross, C.A. Differential cellular expression of isoforms of inositol 1,4,5-triphosphate receptors in neurons and glia in brain. *J. Comp. Neurol.* **1999**, *406*, 207–220. [CrossRef]
33. Hertle, D.N.; Yeckel, M.F. Distribution of inositol-1,4,5-trisphosphate receptor isotypes and ryanodine receptor isotypes during maturation of the rat hippocampus. *Neuroscience* **2007**, *150*, 625–638. [CrossRef] [PubMed]
34. Ivanova, H.; Vervliet, T.; Missiaen, L.; Parys, J.B.; De Smedt, H.; Bultynck, G. Inositol 1,4,5-trisphosphate receptor-isoform diversity in cell death and survival. *Biochim. Biophys. Acta (BBA)-Mol. Cell Res.* **2014**, *1843*, 2164–2183. [CrossRef] [PubMed]
35. Koch, P.; Breuer, P.; Peitz, M.; Jungverdorben, J.; Kesavan, J.; Poppe, D.; Doerr, J.; Ladewig, J.; Mertens, J.; Tüting, T.; et al. Excitation-induced ataxin-3 aggregation in neurons from patients with Machado-Joseph disease. *Nature* **2011**, *480*, 543–546. [CrossRef] [PubMed]
36. Hübener, J.; Weber, J.J.; Richter, C.; Honold, L.; Weiss, A.; Murad, F.; Breuer, P.; Wüllner, U.; Bellstedt, P.; Paquet-Durand, F.; et al. Calpain-mediated ataxin-3 cleavage in the molecular pathogenesis of spinocerebellar ataxia type 3 (SCA3). *Hum. Mol. Genet.* **2013**, *22*, 508–518. [CrossRef] [PubMed]
37. Chen, X.; Tang, T.-S.; Tu, H.; Nelson, O.; Pook, M.; Hammer, R.; Nukina, N.; Bezprozvanny, I. Deranged calcium signaling and neurodegeneration in spinocerebellar ataxia type 3. *J. Neurosci.* **2008**, *28*, 12713–12724. [CrossRef]
38. Tang, T.-S.; Slow, E.; Lupu, V.; Stavrovskaya, I.G.; Sugimori, M.; Llinás, R.; Kristal, B.S.; Hayden, M.R.; Bezprozvanny, I. Disturbed Ca^{2+} signaling and apoptosis of medium spiny neurons in Huntington's disease. *Proc. Natl. Acad. Sci. USA* **2005**, *102*, 2602–2607. [CrossRef]
39. Tang, T.-S.; Tu, H.; Chan, E.Y.W.; Maximov, A.; Wang, Z.; Wellington, C.L.; Hayden, M.R.; Bezprozvanny, I. Huntingtin and huntingtin-associated protein 1 influence neuronal calcium signaling mediated by inositol-(1,4,5) triphosphate receptor type 1. *Neuron* **2003**, *39*, 227–239. [CrossRef]
40. Bauer, P.O.; Hudec, R.; Ozaki, S.; Okuno, M.; Ebisui, E.; Mikoshiba, K.; Nukina, N. Genetic ablation and chemical inhibition of IP3R1 reduce mutant huntingtin aggregation. *Biochem. Biophys. Res. Commun.* **2011**, *416*, 13–17. [CrossRef]
41. Liu, J.; Tang, T.-S.; Tu, H.; Nelson, O.; Herndon, E.; Huynh, D.P.; Pulst, S.M.; Bezprozvanny, I. Deranged calcium signaling and neurodegeneration in spinocerebellar ataxia type 2. *J. Neurosci.* **2009**, *29*, 9148–9162. [CrossRef] [PubMed]

42. Li, X.; Zima, A.V.; Sheikh, F.; Blatter, L.A.; Chen, J. Endothelin-1-induced arrhythmogenic Ca^{2+} signaling is abolished in atrial myocytes of inositol-1,4,5-trisphosphate(IP3)-receptor type 2-deficient mice. *Circ. Res.* **2005**, *96*, 1274–1281. [CrossRef] [PubMed]
43. Agulhon, C.; Fiacco, T.A.; McCarthy, K.D. Hippocampal short- and long-term plasticity are not modulated by astrocyte Ca^{2+} signaling. *Science* **2010**, *327*, 1250–1254. [CrossRef] [PubMed]
44. Takata, N.; Mishima, T.; Hisatsune, C.; Nagai, T.; Ebisui, E.; Mikoshiba, K.; Hirase, H. Astrocyte calcium signaling transforms cholinergic modulation to cortical plasticity in vivo. *J. Neurosci.* **2011**, *31*, 18155–18165. [CrossRef]
45. Chen, N.; Sugihara, H.; Sharma, J.; Perea, G.; Petravicz, J.; Le, C.; Sur, M. Nucleus basalis-enabled stimulus-specific plasticity in the visual cortex is mediated by astrocytes. *Proc. Natl. Acad. Sci. USA* **2012**, *109*, E2832–E2841. [CrossRef]
46. Cao, X.; Li, L.-P.; Wang, Q.; Wu, Q.; Hu, H.-H.; Zhang, M.; Fang, Y.-Y.; Zhang, J.; Li, S.-J.; Xiong, W.-C.; et al. Astrocyte-derived ATP modulates depressive-like behaviors. *Nat. Med.* **2013**, *19*, 773–777. [CrossRef]
47. Petravicz, J.; Boyt, K.M.; McCarthy, K.D. Astrocyte IP3R2-dependent Ca^{2+} signaling is not a major modulator of neuronal pathways governing behavior. *Front. Behav. Neurosci.* **2014**, *8*, 384. [CrossRef] [PubMed]
48. Martin-Fernandez, M.; Jamison, S.; Robin, L.M.; Zhao, Z.; Martin, E.D.; Aguilar, J.; Benneyworth, M.A.; Marsicano, G.; Araque, A. Synapse-specific astrocyte gating of amygdala-related behavior. *Nat. Neurosci.* **2017**, *20*, 1540–1548. [CrossRef] [PubMed]
49. Tanaka, M.; Wang, X.; Mikoshiba, K.; Hirase, H.; Shinohara, Y. Rearing-environment-dependent hippocampal local field potential differences in wild-type and inositol trisphosphate receptor type 2 knockout mice. *J. Physiol.* **2017**, *595*, 6557–6568. [CrossRef]
50. Guerra-Gomes, S.; Viana, J.F.; Nascimento, D.S.M.; Correia, J.S.; Sardinha, V.M.; Caetano, I.; Sousa, N.; Pinto, L.; Oliveira, J.F. The Role of Astrocytic Calcium Signaling in the Aged Prefrontal Cortex. *Front. Cell. Neurosci.* **2018**, *12*, 379. [CrossRef]
51. Guerra-Gomes, S.; Cunha-Garcia, D.; Nascimento, D.S.M.; Duarte-Silva, S.; Loureiro-Campos, E.; Sardinha, V.M.; Viana, J.F.; Sousa, N.; Maciel, P.; Pinto, L.; et al. IP3R2 null mice display a normal acquisition of somatic and neurological development milestones. *Eur. J. Neurosci.* **2020**, *54*, 5673–5686. [CrossRef] [PubMed]
52. Dong, Q.-P.; He, J.-Q.; Chai, Z. Astrocytic Ca^{2+} waves mediate activation of extrasynaptic NMDA receptors in hippocampal neurons to aggravate brain damage during ischemia. *Neurobiol. Dis.* **2013**, *58*, 68–75. [CrossRef] [PubMed]
53. Rakers, C.; Petzold, G.C. Astrocytic calcium release mediates peri-infarct depolarizations in a rodent stroke model. *J. Clin. Investig.* **2017**, *127*, 511–516. [CrossRef] [PubMed]
54. Kanemaru, K.; Kubota, J.; Sekiya, H.; Hirose, K.; Okubo, Y.; Iino, M. Calcium-dependent N-cadherin up-regulation mediates reactive astrogliosis and neuroprotection after brain injury. *Proc. Natl. Acad. Sci. USA* **2013**, *110*, 11612–11617. [CrossRef]
55. Saito, K.; Shigetomi, E.; Yasuda, R.; Sato, R.; Nakano, M.; Tashiro, K.; Tanaka, K.F.; Ikenaka, K.; Mikoshiba, K.; Mizuta, I.; et al. Aberrant astrocyte Ca^{2+} signals "AxCa signals" exacerbate pathological alterations in an Alexander disease model. *Glia* **2018**, *66*, 1053–1067. [CrossRef] [PubMed]
56. Li, H.; Xie, Y.; Zhang, N.; Yu, Y.; Zhang, Q.; Ding, S. Disruption of IP3R2-mediated Ca^{2+} signaling pathway in astrocytes ameliorates neuronal death and brain damage while reducing behavioral deficits after focal ischemic stroke. *Cell Calcium* **2015**, *58*, 565–576. [CrossRef]
57. Staats, K.A.; Humblet-Baron, S.; Bento-Abreu, A.; Scheveneels, W.; Nikolaou, A.; Deckers, K.; Lemmens, R.; Goris, A.; Van Ginderachter, J.A.; Van Damme, P.; et al. Genetic ablation of IP3 receptor 2 increases cytokines and decreases survival of SOD1G93A mice. *Hum. Mol. Genet.* **2016**, *25*, 3491–3499. [CrossRef]
58. Petravicz, J.; Fiacco, T.A.; McCarthy, K.D. Loss of IP3 receptor-dependent Ca^{2+} increases in hippocampal astrocytes does not affect baseline CA1 pyramidal neuron synaptic activity. *J. Neurosci.* **2008**, *28*, 4967–4973. [CrossRef]
59. Takata, N.; Nagai, T.; Ozawa, K.; Oe, Y.; Mikoshiba, K.; Hirase, H. Cerebral Blood Flow Modulation by Basal Forebrain or Whisker Stimulation Can Occur Independently of Large Cytosolic Ca^{2+} Signaling in Astrocytes. *PLoS ONE* **2013**, *8*, e66525. [CrossRef]
60. Schallert, T.; Fleming, S.M.; Leasure, J.L.; Tillerson, J.L.; Bland, S.T. CNS plasticity and assessment of forelimb sensorimotor outcome in unilateral rat models of stroke, cortical ablation, parkinsonism and spinal cord injury. *Neuropharmacology* **2000**, *39*, 777–787. [CrossRef]
61. Bouet, V.; Boulouard, M.; Toutain, J.; Divoux, D.; Bernaudin, M.; Schumann-Bard, P.; Freret, T. The adhesive removal test: A sensitive method to assess sensorimotor deficits in mice. *Nat. Protoc.* **2009**, *4*, 1560–1564. [CrossRef]
62. Vergara, J.; DiFranco, M.; Compagnon, D.; Suarez-Isla, B.A. Imaging of calcium transients in skeletal muscle fibers. *Biophys. J.* **1991**, *59*, 12–24. [CrossRef] [PubMed]
63. Agrawal, A.; Suryakumar, G.; Rathor, R. Role of defective Ca^{2+} signaling in skeletal muscle weakness: Pharmacological implications. *J. Cell Commun. Signal.* **2018**, *12*, 645–659. [CrossRef] [PubMed]
64. Staats, K.A.; Bogaert, E.; Hersmus, N.; Jaspers, T.; Luyten, T.; Bultynck, G.; Parys, J.B.; Hisatsune, C.; Mikoshiba, K.; Van Damme, P.; et al. Neuronal overexpression of IP3 receptor 2 is detrimental in mutant SOD1 mice. *Biochem. Biophys. Res. Commun.* **2012**, *429*, 210–213. [CrossRef]
65. Srinivasan, R.; Huang, B.S.; Venugopal, S.; Johnston, A.D.; Chai, H.; Zeng, H.; Golshani, P.; Khakh, B.S. Ca^{2+} signaling in astrocytes from Ip3r2(-/-) mice in brain slices and during startle responses in vivo. *Nat. Neurosci.* **2015**, *18*, 708–717. [CrossRef] [PubMed]
66. Brenner, B. A new concept for the mechanism of Ca+(+)-regulation of muscle contraction. Implications for physiological and pharmacological approaches to modulate contractile function of myocardium. *Basic Res. Cardiol.* **1991**, *86* (Suppl. S3), 83–92. [CrossRef] [PubMed]

67. Zamponi, G.W.; Striessnig, J.; Koschak, A.; Dolphin, A.C. The Physiology, Pathology, and Pharmacology of Voltage-Gated Calcium Channels and Their Future Therapeutic Potential. *Pharmacol. Rev.* **2015**, *67*, 821–870. [CrossRef]
68. Tu, M.K.; Levin, J.B.; Hamilton, A.M.; Borodinsky, L.N. Calcium signaling in skeletal muscle development, maintenance and regeneration. *Cell Calcium* **2016**, *59*, 91–97. [CrossRef]
69. Denk, W.; Strickler, J.H.; Webb, W.W. Two-photon laser scanning fluorescence microscopy. *Science* **1990**, *248*, 73–76. [CrossRef] [PubMed]
70. Gómez, J.; Ñeco, P.; DiFranco, M.; Vergara, J.L. Calcium Release Domains in Mammalian Skeletal Muscle Studied with Two-photon Imaging and Spot Detection Techniques. *J. Gen. Physiol.* **2006**, *127*, 623–637. [CrossRef]
71. Silva-Fernandes, A.; do Carmo Costa, M.; Duarte-Silva, S.; Oliveira, P.; Botelho, C.M.; Martins, L.; Mariz, J.A.; Ferreira, T.; Ribeiro, F.; Correia-Neves, M.; et al. Motor uncoordination and neuropathology in a transgenic mouse model of Machado-Joseph disease lacking intranuclear inclusions and ataxin-3 cleavage products. *Neurobiol. Dis.* **2010**, *40*, 163–176. [CrossRef] [PubMed]
72. Navarrete, M.; Perea, G.; de Sevilla, D.F.; Gómez-Gonzalo, M.; Núñez, A.; Martín, E.D.; Araque, A. Astrocytes Mediate In Vivo Cholinergic-Induced Synaptic Plasticity. *PLoS Biol.* **2012**, *10*, e1001259. [CrossRef] [PubMed]
73. Carter, R.J.; Lione, L.A.; Humby, T.; Mangiarini, L.; Mahal, A.; Bates, G.P.; Dunnett, S.B.; Morton, A.J. Characterization of progressive motor deficits in mice transgenic for the human Huntington's disease mutation. *J. Neurosci.* **1999**, *19*, 3248–3257. [CrossRef]
74. Schallert, T.; Upchurch, M.; Lobaugh, N.; Farrar, S.B.; Spirduso, W.W.; Gilliam, P.; Vaughn, D.; Wilcox, R.E. Tactile extinction: Distinguishing between sensorimotor and motor asymmetries in rats with unilateral nigrostriatal damage. *Pharmacol. Biochem. Behav.* **1982**, *16*, 455–462. [CrossRef] [PubMed]
75. Rogers, D.C.; Fisher, E.M.; Brown, S.D.; Peters, J.; Hunter, A.J.; Martin, J.E. Behavioral and functional analysis of mouse phenotype: SHIRPA, a proposed protocol for comprehensive phenotype assessment. *Mamm. Genome* **1997**, *8*, 711–713. [CrossRef] [PubMed]
76. Teixeira-Castro, A.; Jalles, A.; Esteves, S.; Kang, S.; da Silva Santos, L.; Silva-Fernandes, A.; Neto, M.F.; Brielmann, R.M.; Bessa, C.; Duarte-Silva, S.; et al. Serotonergic signalling suppresses ataxin 3 aggregation and neurotoxicity in animal models of Machado-Joseph disease. *Brain J. Neurol.* **2015**, *138 Pt 11*, 3221–3237. [CrossRef] [PubMed]
77. Duarte-Silva, S.; Neves-Carvalho, A.; Soares-Cunha, C.; Teixeira-Castro, A.; Oliveira, P.; Silva-Fernandes, A.; Maciel, P. Lithium chloride therapy fails to improve motor function in a transgenic mouse model of Machado-Joseph disease. *Cerebellum* **2014**, *13*, 713–727. [CrossRef] [PubMed]
78. Esteves, S.; Duarte-Silva, S.; Naia, L.; Neves-Carvalho, A.; Teixeira-Castro, A.; Rego, A.C.; Silva-Fernandes, A.; Maciel, P. Limited Effect of Chronic Valproic Acid Treatment in a Mouse Model of Machado-Joseph Disease. *PLoS ONE* **2015**, *10*, e0141610. [CrossRef] [PubMed]
79. Duarte-Silva, S.; Neves-Carvalho, A.; Soares-Cunha, C.; Silva, J.M.; Teixeira-Castro, A.; Vieira, R.; Silva-Fernandes, A.; Maciel, P. Neuroprotective Effects of Creatine in the CMVMJD135 Mouse Model of Spinocerebellar Ataxia Type 3. *Mov. Disord.* **2018**, *33*, 815–826. [CrossRef]
80. Esteves, S.; Oliveira, S.; Duarte-Silva, S.; Cunha-Garcia, D.; Teixeira-Castro, A.; Maciel, P. Preclinical Evidence Supporting Early Initiation of Citalopram Treatment in Machado-Joseph Disease. *Mol. Neurobiol.* **2019**, *56*, 3626–3637. [CrossRef]
81. Duarte-Silva, S.; Silva-Fernandes, A.; Neves-Carvalho, A.; Soares-Cunha, C.; Teixeira-Castro, A.; Maciel, P. Combined therapy with m-TOR-dependent and -independent autophagy inducers causes neurotoxicity in a mouse model of Machado–Joseph disease. *Neuroscience* **2016**, *313*, 162–173. [CrossRef] [PubMed]
82. Correia, J.S.; Neves-Carvalho, A.; Mendes-Pinheiro, B.; Pires, J.; Teixeira, F.G.; Lima, R.; Monteiro, S.; Silva, N.A.; Soares-Cunha, C.; Serra, S.C.; et al. Preclinical Assessment of Mesenchymal-Stem-Cell-Based Therapies in Spinocerebellar Ataxia Type 3. *Biomedicines* **2021**, *9*, 1754. [CrossRef] [PubMed]
83. Campos, A.B.; Duarte-Silva, S.; Fernandes, B.; das Neves, S.P.; Marques, F.; Teixeira-Castro, A.; Neves-Carvalho, A.; Monteiro-Fernandes, D.; Portugal, C.C.; Socodato, R.; et al. Profiling Microglia in a Mouse Model of Machado-Joseph Disease. *Biomedicines* **2022**, *10*, 237. [CrossRef] [PubMed]
84. Campos, A.B.; Duarte-Silva, S.; Fernandes, B.; Coimbra, B.; Campos, J.; Monteiro-Fernandes, D.; Teixeira-Castro, A.; Ambrósio, A.F.; Maciel, P. Microglial Depletion Has No Impact on Disease Progression in a Mouse Model of Machado–Joseph Disease. *Cells* **2022**, *11*, 2022. [CrossRef] [PubMed]